

Uncovering Patterns of Brain Activity from EEG Data Consistently Associated with Cybersickness Using Neural Network Interpretability Maps

Jacqueline Yau *

University of Illinois Urbana-Champaign (UIUC)

Katherine J. Mimnaugh *

UIUC

Evan G. Center †

University of Oulu

Timo Ojala †

University of Oulu

Steven M. LaValle †

University of Oulu and UIUC

Wenzhen Yuan *

UIUC

Nancy Amato *

UIUC

Minje Kim *

UIUC

Kara Federmeier *

UIUC

ABSTRACT

Cybersickness poses a serious challenge for users of virtual reality (VR) technology. Consequently, there has been significant effort to track its occurrence during VR use with brain activity through electroencephalography (EEG). However, a significant confound in current methods for detecting sickness from EEG is they do not account for the simultaneous processing of the sickening visual stimulus that is present in the brain data from VR. Using event-related potentials (ERPs) from an auditory stimulus shown to reflect cybersickness impacts, we can more precisely target EEG cybersickness features and use those to achieve better performance in online cybersickness classification. In this article, we introduce a method utilizing trained convolutional neural networks and transformer models and plot interpretability maps from integrated gradients and class activation to give a visual representation of what the model determined was most useful in sickness classification from an EEG dataset consisting of ERPs recorded during the elicitation of cybersickness. Across 12 runs of our method with three different neural networks, the models consistently pointed to a surprising finding: that amplitudes recorded at an electrode placed on the scalp near the left prefrontal cortex were important in the classification of cybersickness. These results help clarify a hidden pattern in other related research and point to exciting opportunities for future investigation: that this scalp location could be used as a tagged feature for better real-time cybersickness classification with EEG. We provide our code at: [anonymized].

Index Terms: Cybersickness, Machine Learning, EEG, ERPs

1 INTRODUCTION

Virtual reality (VR) is an effective medium for training surgeons, educating students, treating pain, and improving mental health [30]. However, the discomfort that develops from using VR devices, cybersickness, precludes extended use and makes it difficult for some individuals to utilize VR at all [12]. As a result, there has been substantial effort in the scientific community to find methods to unobtrusively detect and predict cybersickness using brain activity recorded with electroencephalography (EEG) [11].

Given the complexity of brain data, it is desirable to find features indicative of cybersickness which can be used by machine learning models (ML) for faster and more accurate online classification. However, achieving this requires overcoming considerable hurdles, including limited datasets for training models, data with high inter-subject variability, and confounds in the signal from unrelated brain activity. In this article, we present a comprehensive evaluation of ML models for classifying EEG data, as well as a final feature

*e-mail: {jhyau2, kmimna2, yuanwz, namato, minje, kfederme}@illinois.edu

†e-mail: {evan.center, timo.ojala, steven.lavalle}@oulu.fi

extraction method that addresses the hurdle of having a small data set with our data processing pipeline, high inter-subject variability using individual calibration, and signal confounds using a particular type of brain data. The goal of this work was to determine which electrodes and time periods in the ERP window best helped the model predict whether or not the participant was experiencing cybersickness. With our method, we were able to achieve around 80% average accuracy on the best performing model and determine which features had the highest attribution with interpretability maps.

To address the challenge posed by the EEG data, we first had to resolve the issue of the limited dataset. EEG datasets are often small as a result of significant requirements in terms of time (EEG studies typically take around 3 hours to complete per subject), resources (for the system and per-run consumable costs), challenge (subject impacts like vomiting in the case of cybersickness studies), and limitations (the difficulty in recruiting a sample with high numbers of people who will get sick as often there are non-responders, and making the study extremely sickening poses risks that may not provide acceptable benefit/risk ratios). As a result, EEG datasets, particularly for cybersickness studies, are quite limited, with one review finding that only 18% (6 total) of EEG cybersickness studies had more than 30 participants [11]. Moreover, as we show here, there is substantial variability in the EEG data from each subject, making it difficult for models to generalize.

Another significant hurdle was that at any given time, study-irrelevant processing is happening simultaneously in the brain, making it difficult to untangle meaningful signals from other extraneous signaling. One of those related but confounding sources of activity is from the VR itself: the brain is simultaneously processing discomfort *and* the visual sensory information, including the optic flow that contributes tovection (illusory sensations of self-motion), a significant contributor to cybersickness [25]. To limit this confound, event-related potentials (ERPs) to auditory stimuli occurring during cybersickness can be used. ERPs are generated by exposing research subjects to a repeated stimulus and then examining the activity recorded from EEG during a short period after the stimulus onset [35]. Each sample in ERP data from an auditory stimulus represents a period of consistent neural processing which occurred when the person heard a sound [47], providing a cleaner baseline of signal to be compared across sick and non-sick periods.

Although a constituent ERP element that is sensitive to cybersickness, the auditory P3b, has been discovered [37], there are likely other patterns present in ERP data that reflect cybersickness. However, they could arise from different time points, electrode locations, band power changes, or some combination of the three. Instead of testing the myriad options, ML can be used to detect these latent cybersickness features. Given the sensitivity of ERPs, it is plausible that sickness-related changes in neural activity are present even before users start to report symptoms. Therefore, if we can determine which features to focus on, more sensitive and precise real-time cybersickness detection could be achieved.

In overcoming these obstacles with the EEG data, we are able to present several important contributions here. First, we provide

a feature extraction method (and its code) that highlights which input features from ERP data provide the highest attribution. While much previous ML work has investigated changes in power in frequency bands like alpha and beta (see [11, 71, 74] for review), here we have built an explainable classification method for ERP amplitudes, a much less studied area with better comparison across samples and the ability to eliminate confounds from visual stimuli. Second, given the small number of studies on ERPs and cybersickness [1, 11, 66, 68], and only one dataset with auditory ERPs during cybersickness [37], it was difficult to predict which electrode locations or time periods within the ERP would best help distinguish when cybersickness was occurring. Although the attribution maps displayed complex interactions across electrodes and time, one consistent result from the models pointed to the utility of left prefrontal scalp regions. Though these results are preliminary and further investigation on this trend with larger dataset is warranted, our method provides a way to test this finding with other datasets, as well as provides a feature can be evaluated for its utility in improving classification accuracy for real-time EEG cybersickness detection.

2 BACKGROUND

2.1 Electroencephalography

EEG captures the activity of groups of pyramidal neurons in the cerebral cortex through electrodes that are placed on the scalp [8, 35, 67]. During neurotransmission, local field potentials are generated in extracellular space when neurotransmitters pass through the synapse between adjacent neurons and bind to dendritic receptors, causing ions to flow into or out of the postsynaptic cell. The electrical potential voltage fluctuations from these postsynaptic potentials are instantaneously transmitted to the surface of the scalp, allowing researchers the ability to record brain activity at the exact moment in which those neural impulses occur [35].

One of the downsides to using EEG arises as the result of simultaneously occurring yet experimentally irrelevant activity in multiple cortical areas necessary to carry out sensory, motor, and cognitive functions. Thus, EEG data can appear to be very “noisy,” although the issue is not always due to poor signal-to-noise ratio if biological, equipment, and environmental confounds have been well-controlled [35]. One method that cognitive neuroscientists have used to address this issue involves generating patterns of brain activity in response to a particular stimulus, or ERPs, and then averaging across repetitions to cancel out “noise” (activity that is inconsistent across trials). During data analysis, a window of data is segmented from the continuous raw EEG signal beginning from typically 100 to 200 ms prior to onset and ending one to two seconds after the stimulus. This period of EEG data around the stimulus onset for a single trial is called an epoch. Changes in the signal at the trial and condition (sets of trials within an experimental manipulation) level can reveal novel and consequential insights into the neural and cognitive processes engaged by the stimulus [18, 23, 35, 67]. For example, a positive-going potential that occurs over centro-parietal electrodes beginning as early as 300 ms after an attended stimulus to which participants must make a response, called the P3b, reflects attentional resources and the engagement of working memory [47].

2.2 Cybersickness

When a person uses a virtual reality (VR) head-mounted display (HMD), they sometimes develop feelings of discomfort, called cybersickness [12]. Cybersickness symptoms include nausea, dizziness, headache, and fatigue, among others [10, 12, 54]. If the sensations arise from using VR specifically, this discomfort can be referred to as VR sickness [30]. Theories on the causes for cybersickness include a conflict between the expectation of particular patterns of combinatory incoming sensory information and the patterns of sensory information experienced in that moment [49, 50],

intravestibular imbalances [48], vestibulo-autonomic responses [5, 14, 39], the pose of the head in the virtual environment [44], unexpected sensations of self-motion in the virtual environment [62, 63], postural instability [51], and others [59].

There are a number of contributors to cybersickness. These include hardware, software, environmental, and individual factors [4, 10, 12, 64, 59, 54]. While not everyone that uses VR does get sick, a significant portion of users can develop adverse systems [59, 21, 61]. Although brief, these symptoms can sometimes last from 10 minutes to four hours after exposure in the HMD has ended [20].

There are different ways that cybersickness can be measured, but the most common method is to have research subjects report how they are feeling after exposure with the Simulator Sickness Questionnaire (SSQ) [24]. The SSQ is comprised of 16 symptoms to which participants must give a rating from 0 (none of that symptom) to 3 (severe intensity of that symptom): general discomfort, fatigue, headache, eyestrain, difficulty focusing, increased salivation, sweating, nausea, difficulty concentrating, fullness of head, blurred vision, dizzy (eyes open), dizzy (eyes closed), vertigo, stomach awareness, and burping. Though several concerns about the SSQ have been raised [64], it is still a widely used measure [12] which allows for results comparison against other work.

2.3 Cybersickness Recognition from EEG

One of the many complicating factors in elucidating the neural components that play a role in VR sickness arises from the way in which cybersickness is quantified with the SSQ. The measure was originally developed for pilot trainees using Navy helicopter flight simulators in the 1990’s [24], and, accordingly, the list of symptoms selected for inclusion in the SSQ reflect what most commonly arose from using those devices. As current HMDs bear little resemblance to the simulators utilized 35 years ago, the symptoms experienced now may not be well-captured by the SSQ [64]. Moreover, the 16 symptoms included span a variety of visual, physiological, and cognitive reactions that each produce activation in different areas of the brain. It is no wonder that brain activity associated with several negative reactions would be complex and difficult to parse.

Due to this difficulty in parsing brain activity from multiple overlapping symptoms, we focused on one item from the SSQ (general discomfort) in order to isolate features in the brain activity that were indicative of cybersickness discomfort for the models. Though there have been other studies exploring patterns in EEG frequency characteristics during cybersickness [11, 71, 74], to our knowledge the prior work has not investigated patterns in ERP data specific to the general discomfort symptom.

Numerous works have used machine learning for cybersickness detection from EEG [33, 36, 52, 71]. This usually involves feature extraction before training a classifier. Features extracted are often in the frequency or time-frequency domain relating to power in frequency bands [33, 52, 75, 15, 26, 40]. A combination of EEG features with other modalities like inertial measurement unit for head movement [15] or biosignals like heart rate, blink rate, and electrocardiogram [40] has also been explored. Some works extract time domain features like variance, standard deviation, and number of peaks [36] or principal component analysis (PCA) components [75]. Commonly chosen classifiers are k-Nearest Neighbors (kNN) [75, 26], support vector machine (SVM) [75, 26], naive bayes (NB) [36], linear discriminant analysis (LDA) [26], convolutional neural network (CNN) [6], long short-term memory (LSTM) [15], AdaBoost [33, 36], and more. Another line of work directly interacts with EEG in the time domain without first extracting features, usually with neural networks [6, 32, 34]. For evaluation, we note that leave-one-subject-out k-folds validation is a more rigorous method to determine how well a model can generalize to unseen subject data [15, 6] as opposed to mixing all subjects’ data together for dataset splits. And due to the usually small dataset size, it may be better

to repeat experiments on all possible folds for analysis, rather than using a small k for k -folds. As our goal is to identify interpretable EEG features in the time domain for cybersickness classification, neural networks with an explainability method is our approach.

2.4 EEG Analysis with ML Model Interpretability

Explainable AI to understand ML model decision-making is a field that can help EEG analysis by identifying which features were most useful to push the model's decision in the right direction. An ablation-style analysis can be done by modifying each part of the model and observing changes in accuracy metrics [38]. Since CNNs are often used in EEG analysis, gradient-weighted class activation maps (GradCAM), which extract activations in the feature map from a target convolutional layer, are a common choice [70, 57], often for EEGNet [31]. Saliency maps are another option, which outline features from the input that most contribute to the correct decision [6]. Integrated gradients that calculate the attribution of input features to model prediction is another choice [34]. With the introduction of transformers, especially vision transformer (ViT), attention maps reveal how different parts of an image (or EEG data shaped similarly to an image) influences the ViT's decision [57]. While these features can be useful, as has been noted by [71], care should be exercised in the interpretation of salient features identified by ML models. These features may be correlated with the focus of the classification, but other more highly correlated biomarkers may be overlooked by the models. More assessment is needed to verify the generalizability of the features, for example, with statistical tests and additional datasets. However, the ML models do point to a direction in which further study and investigation can be done.

3 METHODS

3.1 Dataset Description

The data used for these analyses were derived from a sample of 29 participants (17 female and 12 male, mean age 23.1; see [37] for more details about that study). Participants passively viewed two tours through a virtual museum, each twice, in an Oculus Quest 2 headset while their brain activity was recorded with 21 electrodes placed on the surface of the scalp, per Fig. 1. The two tours through the museum differed based on their amount of rotation and forward speed and were shown in a previous study to evoke either mild or moderate amounts of VR sickness [3]. During the sickening museum tours, participants were instructed to listen to a series of beeps and keep a mental count of how many different sounding beeps occurred, a well-established method in neuropsychological research to elicit patterns of brain activity reflective of the amount of reserve attention that is available [47]. Previous research with the dataset [37] found that the amount of attention available during the task was associated with the amount of VR sickness that participants experienced, with greater amounts of sickness associated with less available attention.

For these analyses, ERP windows (epochs associated with each trial) of 800 ms after the participant heard each beep were extracted. Only the trials where the beeps sounded the same (standards) were used as there were more standards and the ERPs to the oddballs were different. The data was referenced to the average of the mastoids and a 200 ms period before stimulus onset was subtracted out from each trial for baseline correction [35]. There were approximately 330 trials per person and the data was sampled at 250 Hz, providing 200 samples per trial in the time domain. Binary classification labels were created based on each user's self-reported intensity for one VR sickness symptom (general discomfort from the SSQ). If participants reported any level of discomfort (score > 0), then the sample was labeled as "sick," else it was "non-sick." Binary classification was chosen instead of four-class because in the dataset only a subset of people felt discomfort (14 of 29), leaving few examples per class where the score > 0 . Therefore, the sick samples could not be further segmented into varying levels of sickness.

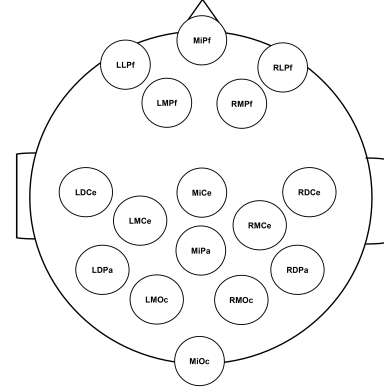


Figure 1: Electrode locations with the front of the head at the top. The electrode names indicate location: R=right, L=left (or L=lateral if second letter), M=medial, D=dorsal, Pf=prefrontal cortex, Ce=centerline, Pa=parietal cortex, Oc=occipital cortex.

3.2 Data Preprocessing

Per the recommendations for preprocessing data from free viewing EEG experiments [17], the raw EEG data was filtered with second-order IIR Butterworth filter with a 12 dB/octave roll-off and a 0.2 to 30 Hz half-amplitude cutoff. Using the extended infomax algorithm for independent component analysis, components associated with artifactual eye movements were removed. Trials with a voltage exceeding $\pm 100 \mu\text{V}$ (38 trials total) were excluded.

3.3 Data Analysis and Augmentation

ML models learn patterns within the train set to generalize to the validation set and unseen test set, so if the train set is skewed or biased in some way, the model could pick up that bias and learn something not inherent in the data. Since the binary classification labels were very skewed (3:1 for non-sick vs sick based on the SSQ symptom general discomfort), we analyzed the data through plots and unsupervised learning, and explored augmentation methods to alleviate this issue. This included balancing the labels through sampling (both over and undersampling), generating synthetic data, and identifying outliers in the data.

Data analysis. Since there was high inter-subject variability in EEG data, we visualized how different each subjects' data was compared to others out of the 29 subjects in the study since we used the more rigorous "leave-one-subject-out" (LOSO) evaluation method where one subject was left out of the train set to be the test set. Plots were made by averaging across the EEG data between sick and non-sick labels and between the 28 subjects vs. the one subject left out, providing a qualitative view of the data (see Fig. 2).

Outlier detection and removal. We considered two kinds of outlier detection: by individual stimuli (individual data point) and by subject. For individual stimuli, original input size is a (C, T) matrix by channel (electrode) C and by time T . We first flattened the data to size $C * T$. Next, the i -th cleaned-up ERP part of the EEG signal \mathbf{x}_i was normalized by z-score, defined as $\mathbf{z}_i = \frac{\mathbf{x}_i - \mu}{\sigma}$ where $\mathbf{x}_i \in \mathbb{R}^{C*T}$ is the flattened vector being normalized, $\mu \in \mathbb{R}^{C*T}$ is the mean, and $\sigma \in \mathbb{R}^{C*T}$ is the standard deviation calculated separately by label for sick vs. non-sick from train set. To clarify, this normalization by separate μ and σ by label is only done for outlier detection analysis. In the main data processing pipeline, the normalization mean and standard deviation are calculated across the whole train set. Along the flattened dimension, if any feature exceeded three standard deviations, it was identified as an outlier and removed from the train set. Since this was quite aggressive, we also tested a milder version that identified outliers if over half the features exceeded three standard deviations. However, test performance dropped, especially

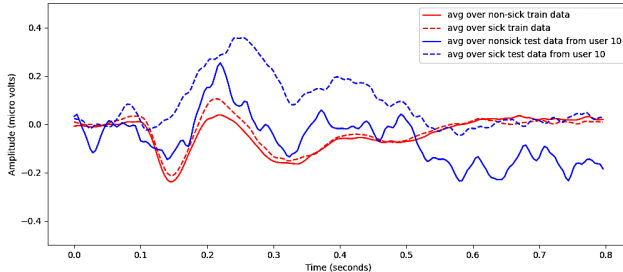


Figure 2: Leaving out Subject 10 from the remaining subjects.

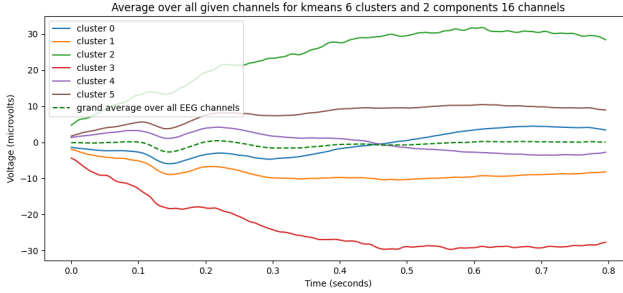


Figure 3: K-means centroids of 6 clusters and average over all data.

on subjects with more sick data, compared to the aggressive version.

For subject outlier detection, we examined the plots from data analysis. For subjects whose data visually looked significantly different from the average of the remaining 28 subjects, we checked the notes from the cybersickness study for a possible explanation. For example, after observing the variation when Subject 10 was left out (Fig. 2), we discovered from the notes that they felt extremely sick to the point of nearly throwing up, whereas the other participants did not feel such an intense level of sickness. Another method used was observing if there were subjects that all models performed poorly on. For example, all models in this work did not evaluate well on Subject 26 prior to calibration. As mentioned in the study notes, Subject 26 had very noisy data from jaw clench muscle contractions. Although there were individuals that deviated quite a bit from the average of the remaining subjects, we did not remove any from the data because these distribution shifts were representative of how different people can and will have EEG variability.

Sampling. To balance the class labels, we tried variations of under and oversampling. For undersampling, we randomly picked majority non-sick data to match the number of sick. For oversampling, we randomly replicated minority sick data until the classes were balanced. These approaches were not ideal, however, since with undersampling we lose data, whereas with oversampling repeating the same data does not provide new information to the models.

Synthetic data for class imbalance. A common method for generating synthetic data is Synthetic Minority Over-sampling Technique (SMOTE) [13]. We explored several variants [28] and found Safe-level SMOTE, which generates synthetic data by using “safe” samples identified by kNN, to be the best fit for our data. We used the smote-variants library [29]. Since SMOTE uses kNN to interpolate synthetic data, it does not work well for high dimensional and noisy data like EEG. In earlier test runs, we observed that neural networks like EEGNet performed better with random oversampling. Thus, SMOTE was not used for the deep learning pipeline.

3.4 Final Data Processing Pipeline

The data processing pipeline used to prepare the dataset for the main deep learning experiments was: 1) outlier detection and removal, 2) normalization, and 3) random oversampling. The aggressive outlier

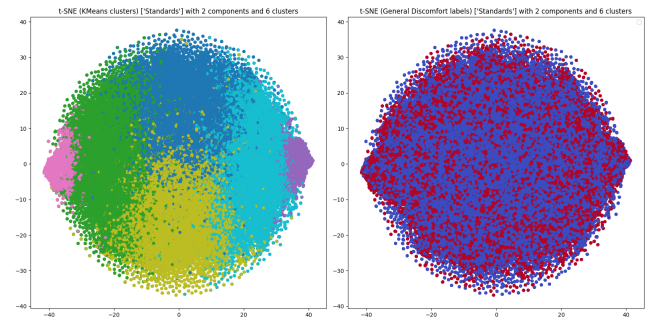


Figure 4: t-SNE for 2 components. Left: data points from the same cluster have the same color. Right: data points are colored based on sick and non-sick label.

detection was run first on the train set, then z-score normalization was done on the remaining data. The validation and test sets were normalized with the same μ and σ obtained from the train set. Finally, the train set was augmented using random oversampling, implemented with the Pytorch’s [45] weighted random sampler by giving higher weights to the minority class data.

3.5 Machine Learning for Pattern Recognition

We considered both supervised and unsupervised learning methods to extract patterns from the data. With supervised learning, both traditional and neural networks were explored. CNN and vision transformers were found to perform the best across the LOSO k-folds, so we focused on those models for interpretation.

Unsupervised learning. Clustering was run to see if any patterns could be identified from individual channel EEG without any labels. We used k-means clustering, where 6 to 7 clusters were found to be the ideal number based on silhouette score [53]. Silhouette score measures inter and intra-cluster distance for each data sample. Each cluster centroid is plotted in Fig. 3. To visualize the high dimensional data, we employed T-distributed Stochastic Neighbor Embedding (t-SNE) [65] for two components, seen in Fig. 4. From the right plot, we can observe that separation between sick and non-sick labeled data is difficult. When decomposing data in each cluster, each subject and electrode had some data in each cluster, indicating that the EEG data were difficult to classify across subjects and electrodes.

Supervised learning with traditional ML models. We tried to find underlying patterns present in the data using the binary sickness labels by comparing traditional ML model performance based on their inductive biases. Though not as powerful as neural networks in capturing complex patterns, traditional models have the advantage of requiring less train data and being more interpretable. We evaluated multiple traditional models with LOSO k-folds cross-validation. The results averaged over all k-folds are shown in Tab. 1. Scikit-learn [46] was used for implementation. The input data was a flattened array of channels C by time T of size $C \times T$. Our pipeline removed outliers and normalized with z-score before running PCA for 48 components.

3.6 Deep Learning

Since traditional ML models struggled to capture the complexities of the EEG data in the time domain, deep learning models were considered. Convolution seemed promising to extract spatially local features in the signal, so EEGNet [31] was chosen as it was designed for EEG data, including ERPs, and compact enough to work with small datasets. Since EEG has a time dimension component, models that take sequential information into account were also considered, specifically transformers. EEG Conformer was chosen as it is a compact convolutional transformer designed to encapsulate local and global features in EEG data [58]. An ImageNet pre-trained

kNN	AdaBoost	RF	LDA	QDA	Bernoulli NB	Gaussian NB	Multinomial NB	SVM	GP	Relu MLP
0.5823	0.6510	0.5566	0.5031	0.5628	0.5066	0.5473	0.4785	0.5983	0.5612	0.6129

Table 1: Average balanced accuracy for traditional ML models across all LOSO k-folds with outlier removal, normalization, PCA, and safe-level SMOTE using the SSQ general discomfort symptom intensity as labels. Results are reported for k=2, 10-tree AdaBoost and random forest (RF) with log loss split criterion, Singular Value Decomposition LDA, quadratic discriminant analysis (QDA), polynomial kernel SVM, and Radial-Basis Function kernel Gaussian Process (GP).

EEG Vision Transformer (ViT) was chosen to leverage the reasoning patterns it had learned from images to EEG data with fine-tuning [73]. Each input data is a matrix of shape electrodes C by time T . All models were implemented in PyTorch.

EEGNet. EEGNet [31] is a two block CNN that has both depthwise convolutions across the channels and temporal convolutions along the time dimension. In the first block is a temporal convolution with kernel size (1,64) and stride 1 along the time dimension, followed by a spatial convolution with kernel size (C , 1) and stride 1 to learn a spatial filter across all electrodes, where C is the number of electrodes. The second block has a separable (depthwise) convolution followed by a pointwise convolution to separate learning how to summarize individual feature maps in time (the depthwise convolution) with how to optimally combine the feature maps (the pointwise convolution) [31]. Finally, a fully-connected layer outputs classification logits.

EEG Conformer. EEG Conformer [58] is a convolutional transformer with three parts: a convolution block for patch embedding, a transformer to learn temporal features, and a classifier block. The patch embedding convolves over the EEG signal similarly to EEGNet’s temporal and spatial convolution, with temporal kernel (1,25) and stride 1, and spatial kernel (C , 1) with stride 1. The learned filters are pooled and rearranged into a sequence of tokens to be passed to the transformer, composed of four encoder blocks. Each encoder block employs multi-head self-attention to learn longer-term temporal features in the token sequence. The self-attention focuses on the relationship between tokens in sequence while multiple heads can represent and capture different kinds of relationships simultaneously. In this work, we use 8 heads and 40 hidden size. The classifier block is composed of three fully-connected layers, outputting classification logits.

Pre-trained EEG ViT. Vision Transformers extract information from an image by decomposing it into a sequence of patch embeddings and extracting temporal information with the transformer blocks. We modified EEG ViT [73] for our task. This model has a patch embedding convolution block, a pre-trained transformer composed of 12 encoder blocks with 12 heads, and a classifier block. It was pre-trained on the ImageNet dataset [16] so it learned to extract patterns from images. Since it was specifically trained on 224×224 size images, decomposed into patches of size 16×16 and has 224 tokens in the patch embedding sequence with 768 hidden size [19], modifications were made to match those dimensions given our EEG input data. Our modified model starts with a temporal convolution of (1,35) with stride 3 and spatial convolution with kernel size (4, 1) to output 224 tokens of 4×1 size patches and the class token for 225 total tokens. The token sequence is passed to the pre-trained ViT backbone and two-layer fully-connected classifier block, outputting classification logits.

3.7 Model Interpretability

Integrated gradients. To visualize which input features the neural network models found helpful (or not) for the model’s classification of the target class label, integrated gradients [60] were extracted using the Captum library [27]. Integrated gradients (IG) is an axiomatic model interpretability algorithm that assigns an importance score to each input feature by approximating the integral of gradients of the model’s output with respect to the inputs along a straight line path from a chosen baseline to the input [27] by accumulating gradients along the path. IG satisfies the completeness

axiom that states attributions add up to the difference between the output of the model F at the input x and the baseline x^0 [60]. It provides a signed value for each input feature, positive attribution for helping the model classify to target label and negative for the reverse. In our method, the baseline was the grand average over all train data (close to zero due to normalization).

GradCAM. Gradient-weighted class activation maps (GradCAM) were extracted with the Pytorch CAM methods library [22]. GradCAM shows which activations in the feature map had more focus for classification of a target label by taking the gradient with respect to the chosen convolution layer’s feature map.

Interpretability for each model. For EEGNet, the final convolution layer was set for GradCAM extraction. The heatmaps show where along the time dimension the activation was strongest for the model to classify sickness. This is because EEGNet’s final convolution layer is a pointwise convolution that mixes all feature maps together. For EEG Conformer and pre-trained EEG ViT, IG provides more fine-grained information about the gradient strength by channel and time. While GradCAM interpretation very much depends on which layer the maps were extracted from, IG passes through the whole model to compute the cumulative gradients.

3.8 Calibration

Due to the high inter-subject variability of the ERP data, it was difficult for the model to generalize to the data of the subject left out. To bridge the domain shift between the train set distribution and the subject left out’s distribution, we used some data of the left out subject to fine-tune the trained model checkpoint (Fig. 5).

Calibration dataset. We sampled either 12.5 or 25% from the dataset of the subject left out. If the subject left out had both labels, then 25% of the data were sampled, where exactly 12.5% were from each class. However, many subjects only had one label, so for those subjects, 12.5% of their data was sampled. To handle the imbalance, the same amount of the other class label were taken from the remaining 28 subjects’ data. Instead of random sampling, we took the top k -nearest neighbors that were closest to the subject left out’s distribution since the goal of the calibration set was to bridge the distribution shift for each individual subject.

The subject left out’s sampled data was projected into a PCA space of 16 components and averaged into a centroid. Next, each of the other label data from the remaining subjects was projected into PCA space and kNN was run to find the data that were closest to the centroid by Euclidean distance. K was the same as 12.5% of the subject left out’s data. Together, this formed the calibration dataset.

The remaining test subject’s data were used as a test set. The validation set was formed by taking 20% of each class from the calibration dataset. Since each subject had about 330 data samples, about 40 for each class label were sampled for calibration. If the test subject only had one label, then about 40 of the other label was taken from the other subjects for a total of 80 data samples, of which approximately 16 were used as validation.

Calibration fine-tuning. Once the calibration dataset was created, the model with the best validation score from the main training phase was selected to be fine-tuned by the calibration set. The validation metric for this phase was a custom weighted balanced accuracy to identify early stopping from evaluation on the validation set, and was designed to have more weight on the correct classification of sick data.

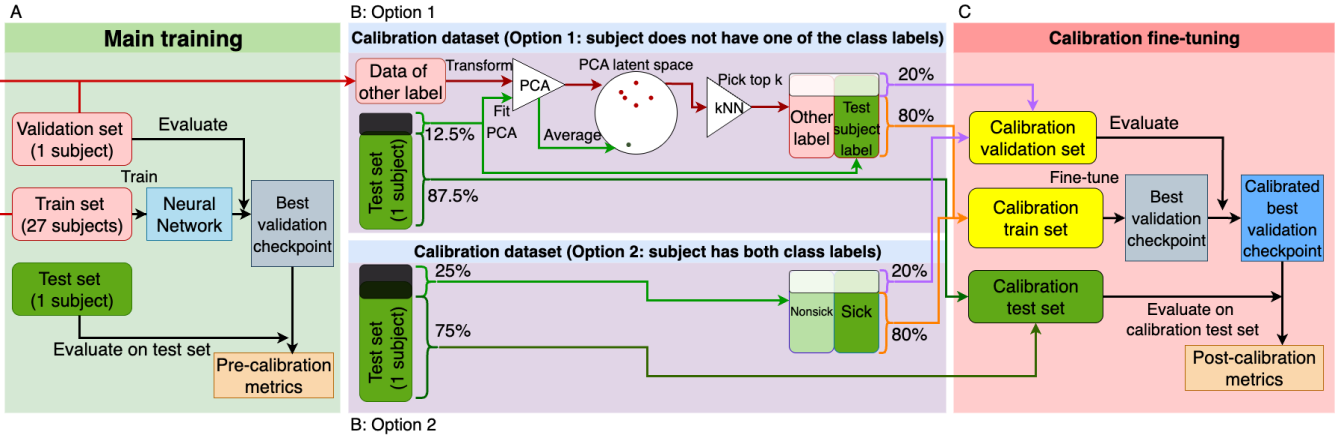


Figure 5: Two-phase process: 1) main training (A) for leave-one-subject-out 1-fold and 2) calibration (B and C) to fine-tune model to the test subject. There are two possible calibration datasets depending on if the test subject data has both labels or not. For main training, the train set goes through outlier detection, z-score normalization, and random oversampling. Best validation checkpoint is fine-tuned in calibration. If test subject has both labels, then 25% of the test subject’s data is sampled. If test subject only has one label, then 12.5% of test subject’s data is sampled and top k data of the other label from other subjects are taken that are closest to sampled test subject data centroid in PCA space.

For EEGNet, all layers were unfrozen to fine-tune all weights. For the EEG Conformer and pre-trained EEG ViT, sections of the model were frozen. For EEG Conformer, the first three of four encoder blocks were frozen. For the pre-trained EEG ViT, all 12 encoder blocks remained frozen. L2-starting point ($L2_{SP}$) [69] regularization, defined in eq. 1 where w_0 is a vector of model parameters from the best validation checkpoint after the main training phase and w is the current model’s unfrozen parameters in the calibration fine-tuning phase and β is the regularization strength, was added to prevent the pre-trained weights from drifting too much during fine-tuning. This was crucial to prevent the model checkpoints from overfitting to the small calibration set and “forgetting” the distribution it had learned during the main training phase. In experiment runs, $\beta = 2e-3$.

$$L2_{SP}(w) = \frac{\beta}{2} \|w - w_0\|^2 \quad (1)$$

Let S be the test subject’s dataset, $b_i = \begin{cases} 2.0 & \text{if } i \in S \\ 1.0 & \text{else} \end{cases}$ be the weight for data sample, $i \in N$ for calibration train set size N , y_i be ground truth label, x_i be the classification output logits, and p_i the softmax probability for the sick label 1 Eq. (2).

$$p_i = \frac{\exp(x_{i,1})}{\exp(x_{i,0}) + \exp(x_{i,1})} \quad (2)$$

$$CE(x, y) = - \sum_{i=1}^N \frac{b_i}{\|b\|} * (y_i \log(p_i) + (1 - y_i) \log(1 - p_i)) \quad (3)$$

We used cross entropy loss (CE) with normalized weight by sample and $L2_{SP}$ regularization to form the calibration phase loss:

$$L(x, y, w) = CE(x, y) + L2_{SP}(w) \quad (4)$$

Custom weighted balanced accuracy. Since we placed more emphasis on the model’s ability to correctly classify sick data at the cost of potentially creating more false positives, we created a custom metric to identify an early train stopping point by validation. This custom weighted balanced accuracy (WBA) allows tuning the weight on the recall of the sick class (positive label) and non-sick class (negative label) while keeping the weights normalized. Let TP be true positive, TN true negative, FP false positive, and FN false negative. In experiment runs, $\alpha = 0.7$.

$$WBA = \alpha * \left(\frac{TP}{TP + FN} \right) + (1 - \alpha) * \left(\frac{TN}{TN + FP} \right) \quad (5)$$

3.9 Experiment Setup

For each model, three trials with different random seeds were run and an additional fourth trial with the channel order re-arranged. For the main training phase, we used an Adam optimizer with learning rate and weight decay of 1×10^{-4} . A multi-step learning rate scheduler was used for EEGNet and EEG Conformer, with milestones at 10,000 and 20,000 steps. For the pre-trained EEG ViT, cosine scheduler with a warmup of 1,000 steps was used, as done by the original model [19]. The batch size was 64. Dropout was 0.25 for both EEGNet and EEG Conformer while pre-trained EEG ViT was 0.1. Cross entropy loss was used (focal loss was tested with the class label imbalance but with random oversampling to balance each batch, cross entropy was found to perform better). For EEGNet and EEG Conformer, the models were trained from scratch. For the pre-trained EEG ViT, fine-tuning was run where the 12 encoder blocks were frozen while the initial convolution and batchnorm, patch embedding, and final classifier layers were unfrozen. For the transformer models, gradient clipping was applied to stabilize training. Balanced accuracy was the metric used in validation to determine early stopping point.

Next was calibration, where the best validation checkpoint for each model for each subject left out was fine-tuned on the smaller calibration dataset with a constant learning rate of 1×10^{-5} . Cross entropy loss was weighted per sample (Eq. (3)), where data from the test subject had double the weight of the data from the others for subjects who only had one label. A custom weighted balanced accuracy (Eq. (5)) was used to determine early stopping points.

The EEGNet and EEG Conformer experiments were run with an Nvidia RTX 4060 GPU while the pre-trained EEG ViT experiments were run on an Nvidia RTX 4090 on Ubuntu Linux computers.

3.10 Metrics

To evaluate our approach in the main training phase, we modified the “leave-one-subject-out” k-folds cross-validation method mentioned earlier, such that one specific subject was left out of the train set to serve as the test set and another subject is randomly chosen to serve as the validation set. The remaining 27 subjects were in the train set. This ensured that the test set was completely unseen by

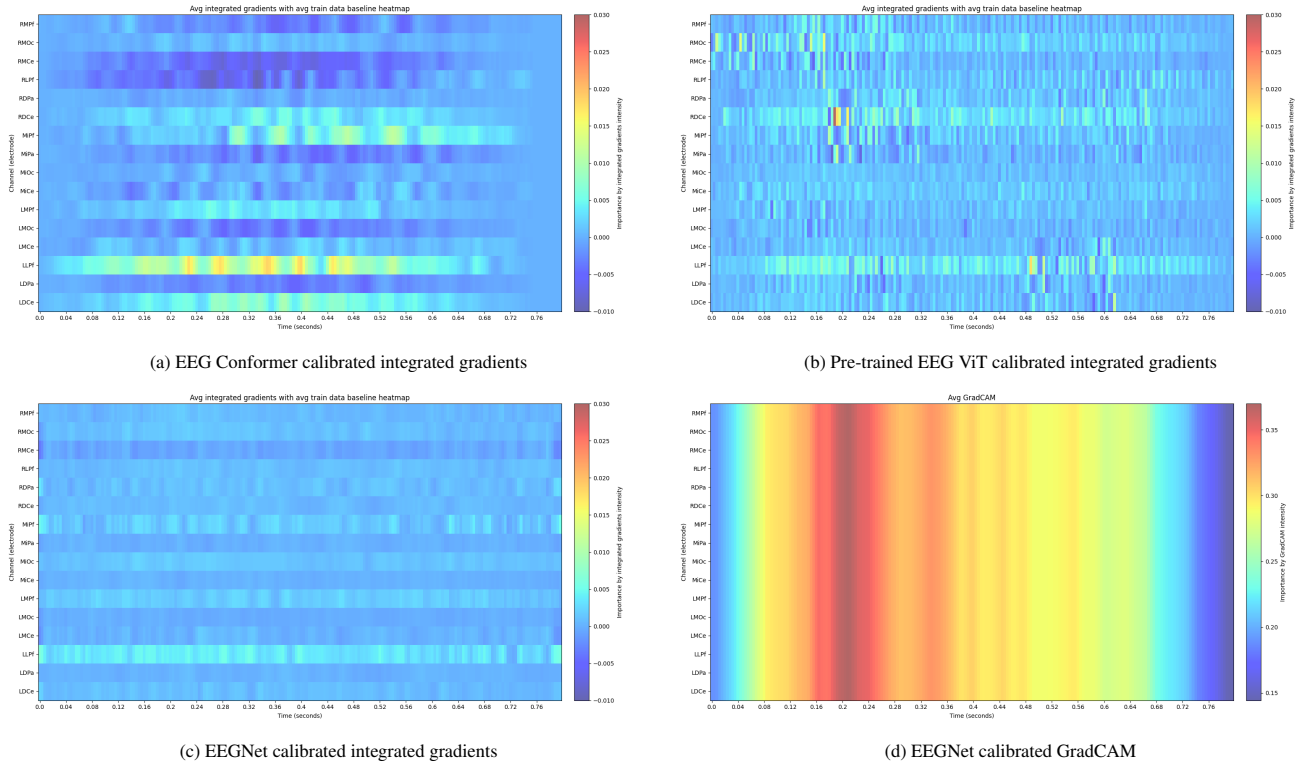


Figure 6: IGs for calibrated models and GradCAM for EEGNet averaged over sick data from subjects with balanced accuracy $> 75\%$.

the model and the evaluation results reflected how well the model could generalize to the unseen subject. For the calibration phase, the validation and test sets were as described in Fig. 5, with the evaluation reflecting how well the model closed the distribution shift to the test subject. Since the dataset was very imbalanced, the metrics we considered are balanced accuracy and F1-score.

Balanced accuracy. Balanced accuracy (BA) is the average of the recall for each class. Let TP be true positive, TN true negative, FP false positive, and FN false negative. Balanced accuracy for binary classification [46] is:

$$BA = \frac{1}{2} \left(\frac{TP}{TP+FN} + \frac{TN}{TN+FP} \right) \quad (6)$$

F1-score. F1-score is the harmonic mean between precision and recall [46], defined as:

$$F1 = \frac{2 * TP}{2 * TP + FP + FN} \quad (7)$$

4 RESULTS

The results from training EEGNet, EEG Conformer, and pre-trained EEG ViT before and after calibration are shown in Tab. 2. For all three models, the calibration phase helped boost the average balanced accuracy and F1-score significantly. EEGNet increased by around 5%, EEG Conformer by 12%, and pre-trained EEG ViT by 23%. Pre-trained EEG ViT performed the best with an average balanced accuracy around 79% and F1-score around 84%. EEG Conformer was close with around a 77% average balanced accuracy and an 82.62% F1-score. EEGNet performed the worst with around a 65% balanced accuracy and 71% F1-score. From the traditional ML model pipeline results in Tab. 1 (like pre-calibration metrics), the highest performing model was Adaboost at 65% balanced accuracy.

The integrated gradients map for all models after calibration, averaged over sick data from high balanced accuracy ($> 75\%$)

subjects for all three runs, is shown in Fig. 6. Results for more runs, including the trial when the models were trained in a different channel order are provided in the Supplemental Material. In terms of the most relevant features for the models, from the IG maps a prominent observation is that across multiple runs and models, some electrodes consistently had high integrated gradient attributions. LLpF had the highest integrated gradients for all models and runs, followed by LDce and RDce. LMPf and MiPf were also generally helpful for the models with a higher average sum of IG. In the time domain, in EEG Conformer’s IG map for LLpF there were time steps highlighted between 240 to 440ms, while EEGNet’s GradCAM highlighted an earlier 160 to 240ms window. Pre-trained EEG ViT highlighted around 160 to 200ms for LLpF and RDce. Tab. 3 shows the sum of integrated gradients across channels and averaged by model over all experiment runs.

5 DISCUSSION

In this paper, we present a method to determine which features for machine learning models were most important in classifying signals from small imbalanced datasets with high variability between data sources. While some constituent components of certain event-related potentials have been elucidated, there are likely many other patterns of neural activity present in the brain data that have not yet been detected. To uncover these patterns, the method presented here utilizes CNNs and transformer models, calibration per data source, and interpretability maps to provide a visual representation of what the models focused on when classifying the signal. Using a limited sample (29 participants) of brain activity from ERP data occurring while participants experienced a stimulus that caused cybersickness in some cases, we compared the highest ranked features between a CNN (EEGNet), a convolutional transformer (EEG Conformer), and a pre-trained vision transformer (EEG ViT). We found areas of the head (left frontal and lateral central) that best helped predict if the sample occurred during a period of sickness or not. These features can be used to improve the accuracy of cybersickness classification

Subject	Pre-calibration								Post-calibration								Sick %
	EEGNet				Conformer				Pretrained ViT				EEGNet				Sick %
	BA	F1	BA	F1	BA	F1	BA	F1									
0	48.10 \pm 2.36	62.10 \pm 2.26	50.79 \pm 7.91	59.06 \pm 5.50	49.47 \pm 2.66	61.05 \pm 4.16	49.16 \pm 7.78	62.23 \pm 5.14	53.92 \pm 8.94	56.81 \pm 13.32	54.83 \pm 6.62	59.43 \pm 6.79	74.38				
1	90.78 \pm 8.16	95.08 \pm 4.59	96.11 \pm 3.43	98.00 \pm 1.79	75.69 \pm 6.94	86.07 \pm 4.48	77.61 \pm 11.06	87.17 \pm 7.26	91.64 \pm 1.09	82.14 \pm 4.97	90.15 \pm 2.96	0.0					
2	58.94 \pm 13.79	73.81 \pm 11.60	69.77 \pm 13.26	81.69 \pm 9.04	41.21 \pm 17.27	57.57 \pm 18.94	62.28 \pm 4.84	76.70 \pm 3.73	76.99 \pm 17.82	86.50 \pm 10.84	84.08 \pm 8.65	91.26 \pm 5.26	0.0				
3	96.36 \pm 3.03	98.14 \pm 1.59	57.12 \pm 31.97	69.01 \pm 25.22	87.12 \pm 6.52	93.06 \pm 3.79	94.12 \pm 6.57	96.92 \pm 3.56	85.73 \pm 10.12	92.21 \pm 5.67	94.72 \pm 3.20	97.28 \pm 1.67	1.0				
4	70.61 \pm 13.33	82.46 \pm 9.62	81.89 \pm 4.47	90.02 \pm 2.67	61.44 \pm 4.17	76.07 \pm 3.24	72.15 \pm 13.67	83.55 \pm 9.75	90.92 \pm 5.28	95.21 \pm 2.85	87.80 \pm 3.37	93.49 \pm 1.93	0.0				
5	95.39 \pm 10.20	97.54 \pm 5.54	94.56 \pm 3.63	97.19 \pm 1.90	80.66 \pm 9.06	89.16 \pm 5.71	93.97 \pm 5.34	96.85 \pm 2.88	87.07 \pm 3.97	93.07 \pm 2.30	80.95 \pm 6.47	89.41 \pm 4.03	0.0				
6	57.05 \pm 6.29	72.57 \pm 4.98	75.68 \pm 7.20	86.04 \pm 4.74	50.30 \pm 16.06	66.27 \pm 15.26	61.94 \pm 16.61	75.87 \pm 13.49	86.33 \pm 14.71	92.42 \pm 8.95	80.02 \pm 4.24	88.87 \pm 2.65	0.0				
7	23.87 \pm 27.49	36.06 \pm 31.80	41.47 \pm 17.45	57.53 \pm 16.61	45.85 \pm 8.38	62.69 \pm 8.19	29.48 \pm 7.07	45.35 \pm 8.73	82.59 \pm 13.97	90.03 \pm 8.64	81.55 \pm 3.97	89.82 \pm 2.38	0.0				
8	91.44 \pm 17.80	95.18 \pm 10.37	71.97 \pm 11.06	83.52 \pm 7.21	85.68 \pm 12.05	92.09 \pm 7.27	94.55 \pm 5.45	97.16 \pm 2.84	84.34 \pm 14.10	91.25 \pm 8.73	89.40 \pm 8.52	94.38 \pm 4.57	1.0				
9	54.46 \pm 36.18	66.44 \pm 28.64	78.70 \pm 17.37	87.28 \pm 11.25	22.96 \pm 4.53	37.19 \pm 6.06	66.90 \pm 26.55	79.06 \pm 17.55	92.67 \pm 7.16	96.10 \pm 3.91	97.50 \pm 2.16	98.73 \pm 1.10	0.0				
10	58.06 \pm 2.19	44.95 \pm 11.29	57.40 \pm 1.36	32.72 \pm 3.63	55.49 \pm 3.34	47.18 \pm 12.00	59.97 \pm 3.12	53.80 \pm 8.55	63.82 \pm 6.23	54.46 \pm 3.54	57.60 \pm 6.15	61.68 \pm 4.17	0.7515				
11	49.36 \pm 2.42	45.23 \pm 8.69	53.08 \pm 2.04	49.75 \pm 1.55	49.56 \pm 1.94	48.52 \pm 0.31	50.09 \pm 4.70	47.26 \pm 5.42	54.67 \pm 6.37	53.20 \pm 7.32	52.75 \pm 5.13	52.60 \pm 5.04	0.5061				
12	55.06 \pm 18.81	70.32 \pm 17.11	77.87 \pm 7.48	87.45 \pm 4.82	62.23 \pm 11.48	76.48 \pm 9.14	57.84 \pm 11.12	73.09 \pm 8.54	74.83 \pm 19.31	84.88 \pm 12.10	89.91 \pm 4.05	94.67 \pm 2.28	0.0				
13	31.50 \pm 14.12	47.17 \pm 15.49	8.16 \pm 1.51	15.07 \pm 2.60	33.76 \pm 16.99	49.68 \pm 17.65	65.34 \pm 24.66	77.93 \pm 20.09	70.60 \pm 8.02	82.68 \pm 5.35	86.03 \pm 6.72	92.44 \pm 3.81	1.0				
14	48.43 \pm 4.16	52.49 \pm 7.01	49.97 \pm 2.74	51.21 \pm 5.98	47.57 \pm 0.76	58.87 \pm 4.35	50.88 \pm 2.89	54.30 \pm 6.67	52.28 \pm 3.84	54.75 \pm 11.1	50.97 \pm 3.33	57.36 \pm 2.80	0.7523				
15	48.16 \pm 7.29	61.64 \pm 9.96	49.14 \pm 2.11	64.64 \pm 1.77	47.40 \pm 1.16	62.27 \pm 1.35	47.76 \pm 5.02	58.69 \pm 17.02	51.80 \pm 9.54	64.49 \pm 3.43	53.19 \pm 3.81	57.27 \pm 6.32	0.2455				
AVG	60.71 \pm 2.36	65.93 \pm 1.44	64.18 \pm 2.36	70.07 \pm 1.95	56.50 \pm 0.58	64.14 \pm 1.09	64.96 \pm 2.76	71.71 \pm 2.92	77.24 \pm 1.60	82.82 \pm 1.00	79.11 \pm 1.40	84.00 \pm 0.74	0.3530				

Table 2: Balanced accuracy (BA) and F1-score percentages across all models for each subject as test set in leave-one-subject-out cross-validations with outlier removal and random oversampling using the SSQ “general discomfort” symptom intensity as labels. Metrics before and after calibration are shown. Sick % refers to the percentage of trials for that individual where they reported feeling some discomfort.

Electrode	EEGNet	Conformer	Pre-trained ViT	Avg
LDCe	0.320	1.374	0.258	0.651
LDPa	0.075	-0.120	0.156	0.037
LLPf	0.814	1.790	0.700	1.101
LMCe	0.052	0.217	0.003	0.091
LMOc	-0.066	-0.195	0.331	0.023
LM Pf	0.392	0.417	0.198	0.336
MiCe	-0.112	-0.156	0.214	-0.018
MiOc	0.182	0.275	0.140	0.199
MiPa	0.017	-0.393	0.250	-0.042
MiPf	0.384	0.401	0.258	0.348
RD Ce	0.184	0.737	0.687	0.536
RD Pa	0.178	0.009	0.154	0.114
RL Pf	0.088	-0.198	0.307	0.066
RM Ce	-0.248	-0.682	0.015	-0.305
RM Oc	0.146	0.249	0.246	0.214
RM Pf	0.119	-0.186	0.156	0.030

Table 3: Average of the sum of integrated gradients (IGs) across time for each electrode channel for all trials.

and provide testable hypotheses on cybersickness-related impacts on auditory ERP processing in the future.

From the metrics, calibration did significantly improve the models’ classification performance and from the IG maps and sum across each channel, certain electrodes were consistently important across multiple models and runs. Comparing the traditional ML performance to pre-calibration average results, Adaboost with 10 trees, fitted on 28 subjects’ data, performed better than the neural network models trained on 27 subjects, with EEG Conformer having similar balanced accuracy. However, calibration fine-tuning with transfer learning was not possible for Adaboost. Perhaps Adaboost could be trained on the union of the main and calibration train sets but it cannot leverage pattern transfer like neural networks can.

Based on the metrics increase post-calibration, it seems having some way to bridge the distribution shift between train set and test subjects, especially when working with a small dataset of complex and noisy data like EEG, is crucial for tailoring a classifier to an individual for cybersickness detection. Since the transformers performed better than EEGNet after calibration, this may indicate that the temporal features the transformers take into account with

attention in the encoder blocks are important for cybersickness detection in EEG data, which EEGNet as a CNN only, lacks.

Even though calibration does help improve metrics, the subjects with both labels were harder for the models. This may be because the distribution shift was larger between these subjects and the others in the train set where the majority of subjects only had one label. Reducing the $L2_{SP}$ regularization may allow the models to calibrate more to these subjects, though there is a trade-off of possibly losing helpful patterns learned from other subjects. Alternatively, training the model on the subject’s data only or supplementing with data from more people may help.

Another notable observation is that when the models were trained on a different order of channels, the metrics were similar. This is interesting for pre-trained EEG ViT which has a spatial convolution over four channels. While electrode locations and ordering are important, the similar average balanced accuracy indicates that electrode spatial location did not have as much effect for the model to classify cybersickness. However, the channels marked as important by IG remained consistent even with a different order. Thus, the relative location between channels may not have been as important for cybersickness detection as the channel itself for these models. In contrast to the typical montage, here the electrodes were spaced equidistantly providing more even coverage.

Given the frequency with which it occurs and the harmful impacts that result, tracking cybersickness from brain activity as it is happening would enable doctors, patients, teachers, and trainees to derive even greater benefits from the use of immersive technology. A significant barrier to achieving this goal relates to the ambiguity in current knowledge on the neural correlates of discomfort. A review of 33 studies on brain activity during cybersickness measured by EEG found associated changes in every frequency band and across broad areas of the head [11]. This substantial body of conflicting evidence makes it difficult to determine which features would best help classify cybersickness. Here, we extracted features from only the subjects who experienced cybersickness and were highly accurately labeled. Thus, our features are from a small number of people: five for Conformer, five for EEGNet, and six for pretrained EEG ViT. Although this does decrease the amount of contributing data, we have greater confidence that the selected features actually reflect something about cybersickness discomfort classification and not other patterns present in the data. This may explain why a

fewer number of features were especially important in our paper as compared to other work. Indeed, when we compared the most useful features between high accuracy sick subjects and all subjects where the majority are non-sick, the IGs both within multiple runs of the same neural network and between different neural networks show incongruent results, making it difficult to find consistent features.

Amplitudes recorded at the scalp are comprised of mixtures of activity from multiple neuronal aggregates generating signals over periods of time from a few to hundreds of milliseconds. As a result, the amplitudes recorded at any specific time point will be highly correlated with other amplitudes that are temporally and spatially adjacent. Therefore, it could be reasonably expected that features in the IG maps would show gradients ramping up and down from time periods or electrode areas of peak relevance. With this in mind, when we examined features in the time dimension, there were not any readily apparent consistent patterns. GradCAM for EEGNet showed a gradient in importance peaking around 200 ms, but this result would fit with what would be expected about early sensory processing. It takes at least 20 ms for the signal from the sound waves reaching the eardrum to pass through the auditory nerve, brainstem, midbrain, thalamus, and then into the auditory cortex and other areas nearer to the skull, from where we could reasonably expect to pick up activity in scalp electrodes. Components associated with auditory processing typically evaluated begin around 50 ms after the stimulus, with early sensory components like the N1 reflecting processing of basic features of the sound. The latency of these early auditory components would be the most consistent in timing across subjects during early periods after the stimulus and tapering off through the rest of the ERP window, as the GradCAM shows.

Across the models and runs, even with a different channel order, LLPf was consistently the channel with highest integrated gradients, meaning that the left frontal scalp region helped in distinguishing discomfort. This result harmonizes with previous research and helps narrow in on an important component of cybersickness: the feeling of discomfort. Yang, Kasaboc, and Cakmak [72] also found that activity in nearby a left frontal electrode site above the inferior frontal gyrus was an important feature in predicting cybersickness. Other studies have found beta power in left frontal regions to be important in cybersickness classification as well [26, 42]. Thus, we postulate that tagging the left frontal region as a feature may be useful for online cybersickness detection.

After LLPf, the other channels that had the highest IGs across time in all the models were the electrodes LDCE, RDCE, LMPf, and MiPf. LDCE, which sits on a central area on the side of the head above the left ear, had the second highest IG score. MiPf sits at the midline of the cerebral hemispheres above the prefrontal cortex on the forehead, and the left medial prefrontal electrode (LMPf) and MiPf are in close proximity to LLPf. Together with LDCE, these electrodes cover an ovoid area on the left frontal region of the head. It is possible that patterns of activity in this region together could have provided cybersickness-related information to the models, but is difficult to say with certainty. This lateralized pattern is interesting as it is often the case that relevant processing occurs in mirrored areas on both sides of the head, as is the case with LDCE and RDCE. Here, EEG was not recorded from frontal areas between the prefrontal electrodes and centerline electrodes. As such, it is unclear whether electrodes in that left frontal area, corresponding roughly to F7 and F3 in 10/20 layouts, would also have been useful.

It is important to note that signals from activity in different brain areas are distorted as they pass through the skull and meninges and propagate across the head. Additionally, the amplitudes that are picked up from an individual electrode can reflect the combination of activity from numerous neuronal ensembles, including those at some distance, making it difficult to map between (two-dimensional) scalp space and (three-dimensional) brain space (the EEG inverse problem [35]). This makes it very challenging to determine where in

the brain the signals we record with EEG are coming from. It is also difficult to determine with certainty what it was about the patterns in the original signal that the models were picking up on after convolution. As such, care should be exercised in translating from ML model features to characteristics of underlying brain activity.

For this reason, we cannot interpret with certainty the neural or functional significance of the pattern in amplitudes above left frontal areas that were here determined as an important feature by our models. At the same time, it is interesting to note what is known about the activity in left frontal and prefrontal areas from fMRI research (which can give definitive answers on activity in specific brain regions) regarding pain and sickness processing. Prior work has pointed to the prefrontal and orbitofrontal cortices as areas involved in regulation of autonomic outflow [55], and nausea induced fromvection stimulation during fMRI has been shown to result in activation in frontal areas [41]. Moreover, activity in the left dorsolateral prefrontal cortex (DLPFC) and left ventrolateral prefrontal cortex were significantly correlated with autonomic reactions (change in skin conductance) during recovery fromvection-induced nausea [55], further implicating vestibulo-autonomic responses in cybersickness [5, 14, 39].

Furthermore, the consequential role of a frontal area (the DLPFC) in pain regulation and suppression, especially for headache, has been well-established [2, 43, 56]. Abnormalities in the DLPFC have been found in patients with chronic back pain [43] and migraines [76], and the relationship between migraines [56, 76] and cybersickness has been investigated previously [9]. Interestingly, transcranial magnetic stimulation (TMS) to the left DLPFC specifically has been demonstrated as an effective treatment for thermal pain [7] and migraine [76]. In view of this, it would be interesting to explore if TMS to the left DLPFC could reduce discomfort from cybersickness.

6 LIMITATIONS AND FUTURE WORK

Though we have shown our method can handle this cybersickness dataset, it is small for ML, even if that is expected for EEG datasets. Another limitation is that there were no pre-central frontal electrodes, so the electrode montage has a gap in that region. Also, the labels for this dataset are quite coarse since the SSQ was given to subjects after a block of trials, though this is standard for cybersickness measurement [11]. Since the classification accuracy was not $> 75\%$ for some subjects, there may have been some other features that the models missed as well. While we have explored CNNs and transformers to learn patterns from the EEG data, these models had no information about the distance between electrodes. Keeping track of the electrode montage as an adjacency matrix with graph convolution networks (GCN) is another possible future direction. Especially with how brain signals propagate over the head, GCNs could represent that behavior through message propagation.

7 CONCLUSION

EEG is a useful tool for real-time cybersickness detection as people interact in VR. We introduce a method to train and calibrate CNN and transformer models to classify cybersickness given a short window of ERP data. Our method also extracts interpretable features with integrated gradients to highlight which features were most salient for the model to classify sickness. We found an electrode above a left frontal region of the brain was most important for all the models across multiple runs. Future work will include verifying the extracted features on another dataset, exploring time-frequency analysis of the EEG, and using GCNs to capture the structure between electrodes that CNNs cannot.

ACKNOWLEDGMENTS

The authors wish to thank Markku Suomalainen, Israel Becerra, Rafael Murrieta-Cid, Eliezer Lozano, Abdulsatar Aboud, Michael Mimnaugh, James Motes, and Marco Morales.

REFERENCES

[1] M.-H. Ahn, J. H. Park, H. Jeon, H.-J. Lee, H.-J. Kim, and S. K. Hong. Temporal dynamics of visually induced motion perception and neural evidence of alterations in the motion perception process in an immersive virtual reality environment. *Frontiers in Neuroscience*, 14(November):1–9, Nov. 2020. doi: 10.3389/fnins.2020.600839 2

[2] A. V. Apkarian, M. C. Bushnell, R. D. Treede, and J. K. Zubieta. Human brain mechanisms of pain perception and regulation in health and disease. *European Journal of Pain*, 9(4):463, 2005. doi: 10.1016/j.ejpain.2004.11.001 9

[3] I. Becerra, M. Suomalainen, E. Lozano, K. J. Mimnaugh, R. Murrieta-Cid, and S. M. LaValle. Human perception-optimized planning for comfortable vr-based telepresence. *IEEE Robotics and Automation Letters*, 5(4):6489–6496, Oct. 2020. doi: 10.1109/LRA.2020.3015191 3

[4] N. Biswas, A. Mukherjee, and S. Bhattacharya. “are you feeling sick?” – a systematic literature review of cybersickness in virtual reality. *ACM Computing Surveys*, 56(11):1–38, Nov. 2024. doi: 10.1145/3670008 2

[5] J. M. Bogle, E. Benarroch, and P. Sandroni. Vestibular-autonomic interactions: Beyond orthostatic dizziness. *Curr. Opin. Neurol.*, 35(1):126–134, 2022. doi: 10.1097/WCO.0000000000001013 2, 9

[6] D. Borra, E. Magosso, et al. Deep learning-based eeg analysis: investigating p3 erp components. *Journal of Integrative Neuroscience*, 20(4):791–811, 2021. 2, 3

[7] F. Brighina, M. De Tommaso, F. Giglia, S. Scalia, G. Cosentino, A. Puma, M. Panetta, G. Giglia, and B. Fierro. Modulation of pain perception by transcranial magnetic stimulation of left prefrontal cortex. *Journal of Headache and Pain*, 12(2):185–191, 2011. doi: 10.1007/s10194-011-0322-8 9

[8] G. Buzsáki, C. A. Anastassiou, and C. Koch. The origin of extracellular fields and currents-eeg, ecog, ifp and spikes. *Nature Reviews Neuroscience*, 13(6):407–420, 2012. doi: 10.1038/nrn3241 2

[9] G. F. Carvalho, J. Mehnert, H. Basedau, K. Luedtke, and A. May. Brain processing of visual self-motion stimuli in patients with migraine: An fmri study. *Neurology*, 97(10):E996–E1006, 2021. doi: 10.1212/WNL.00000000000012443 9

[10] P. Caserman, A. Garcia-Agundez, A. Gámez Zerban, and S. Göbel. Cybersickness in current-generation virtual reality head-mounted displays: systematic review and outlook. *Virtual Reality*, 25(4):1153–1170, 2021. doi: 10.1007/s10055-021-00513-6 2

[11] E. Chang, M. Billinghamst, and B. Yoo. Brain activity during cybersickness: A scoping review. *Virtual Reality*, 2023. doi: 10.1007/s10055-023-00795-y 1, 2, 8, 9

[12] E. Chang, H. T. Kim, and B. Yoo. Virtual reality sickness: A review of causes and measurements. *International Journal of Human–Computer Interaction*, 36(17):1658–1682, Oct. 2020. doi: 10.1080/10447318.2020.1778551 1, 2

[13] N. V. Chawla, K. W. Bowyer, L. O. Hall, and W. P. Kegelmeyer. Smote: Synthetic minority over-sampling technique. *Journal of Artificial Intelligence Research*, 16:321–357, June 2002. doi: 10.1613/jair.953 4

[14] B. Cohen, M. Dai, S. B. Yakushin, and C. Cho. The neural basis of motion sickness. *Journal of Neurophysiology*, 121(3):973–982, 2019. doi: 10.1152/jn.00674.2018 2, 9

[15] B. U. Demirel, A. H. Dogan, J. Rossie, M. Möbus, and C. Holz. Beyond subjectivity: Continuous cybersickness detection using eeg-based multitaper spectrum estimation. *IEEE Transactions on Visualization and Computer Graphics*, 31(5):2525–2534, 2025. doi: 10.1109/TVCG.2025.3549132 2

[16] J. Deng, W. Dong, R. Socher, L.-J. Li, K. Li, and L. Fei-Fei. ImageNet: A Large-Scale Hierarchical Image Database. In *CVPR09*, 2009. 5

[17] O. Dimigen. Optimizing the ica-based removal of ocular eeg artifacts from free viewing experiments. *NeuroImage*, 207(November 2019):116117, 2020. doi: 10.1016/j.neuroimage.2019.116117 3

[18] E. Donchin. Surprise!...surprise? *Psychophysiology*, 18:493–513, 1981. doi: 0048-5772/81/050493-21 2

[19] A. Dosovitskiy, L. Beyer, A. Kolesnikov, D. Weissenborn, X. Zhai, T. Unterthiner, M. Dehghani, M. Minderer, G. Heigold, S. Gelly, J. Uszkoreit, and N. Houlsby. An image is worth 16x16 words: Transformers for image recognition at scale, 2021. 5, 6

[20] N. Dużmańska, P. Strojny, and A. Strojny. Can simulator sickness be avoided? a review on temporal aspects of simulator sickness. *Frontiers in Psychology*, 9(NOV), Nov. 2018. doi: 10.3389/fpsyg.2018.02132 2

[21] L. E. Garrido, M. Frías-Hiciano, M. Moreno-Jiménez, G. N. Cruz, Z. E. García-Batista, K. Guerra-Peña, and L. A. Medrano. Focusing on cybersickness: pervasiveness, latent trajectories, susceptibility, and effects on the virtual reality experience. *Virtual Reality*, 26(4):1347–1371, 2022. doi: 10.1007/s10055-022-00636-4 2

[22] J. Gildenblat and contributors. Pytorch library for cam methods. <https://github.com/jacobgil/pytorch-cam>, 2021. 5

[23] S. A. Hillyard and M. Kutas. Electrophysiology of cognitive processing. *Annual Review of Psychology*, 34(1):33–61, Jan. 1983. doi: 10.1146/annurev.ps.34.020183.000341 2

[24] R. S. Kennedy, N. E. Lane, K. S. Berbaum, and M. G. Lilienthal. Simulator sickness questionnaire: An enhanced method for quantifying simulator sickness. *The International Journal of Aviation Psychology*, 3(3):203–220, July 1993. doi: 10.1207/s15527108ijap0303_3 2

[25] B. Keshavarz, B. E. Riecke, L. J. Hettinger, and J. L. Campos.vection and visually induced motion sickness: How are they related? *Frontiers in Psychology*, 6:1–11, Apr. 2015. doi: 10.3389/fpsyg.2015.00472 1

[26] A. Z. Khoirunnisa, E. S. Pane, A. D. Wibawa, and M. H. Purnomo. Channel selection of eeg-based cybersickness recognition during playing video game using correlation feature selection (cfs). *International Conference on Biomedical Engineering: Smart Technology for Better Society*, p. 48–53, 2018. doi: 10.1109/BIOMED.2018.8534877 2, 9

[27] N. Kokhlikyan, V. Miglani, M. Martin, E. Wang, B. Alsallakh, J. Reynolds, A. Melnikov, N. Kliushkina, C. Araya, S. Yan, and O. Reblitz-Richardson. Captum: A unified and generic model interpretability library for pytorch, 2020. 5

[28] G. Kovács. An empirical comparison and evaluation of minority oversampling techniques on a large number of imbalanced datasets. *Applied Soft Computing*, 83:105662, 2019. (IF-2019=4.873). doi: 10.1016/j.asoc.2019.105662 4

[29] G. Kovács. smote-variants: a python implementation of 85 minority oversampling techniques. *Neurocomputing*, 366:352–354, 2019. doi: 10.1016/j.neucom.2019.06.100 4

[30] S. M. LaValle. *Virtual reality*. Cambridge university press, 2023. 1, 2

[31] V. J. Lawhern, A. J. Solon, N. R. Waytowich, S. M. Gordon, C. P. Hung, and B. J. Lance. Eegnet: a compact convolutional neural network for eeg-based brain–computer interfaces. *Journal of Neural Engineering*, 15(5):056013, July 2018. doi: 10.1088/1741-2552/aae8c 3, 4, 5

[32] Y. Lee and M. Alamaniotis. Unsupervised eeg cybersickness prediction with deep embedded self organizing map. In *2020 IEEE 20th International Conference on Bioinformatics and Bioengineering (BIBE)*, pp. 538–542, 2020. doi: 10.1109/BIBE50027.2020.00093 2

[33] X. Li, C. Zhu, C. Xu, J. Zhu, Y. Li, and S. Wu. Vr motion sickness recognition by using eeg rhythm energy ratio based on wavelet packet transform. *Computer methods and programs in biomedicine*, 188:105266, 2020. 2

[34] M. Liu, B. Yang, M. Xu, P. Zan, L. Chen, and X. Xia. Exploring quantitative assessment of cybersickness in virtual reality using eeg signals and a cnn-eca-lstm network. *Displays*, 81:102602, 2024. 2, 3

[35] S. J. Luck. *An introduction to the event-related potential technique*. MIT Press, 2 ed., 2014. 1, 2, 3, 9

[36] M. Mawalid, A. Z. Khoirunnisa, M. H. Purnomo, and A. D. Wibawa. Classification of eeg signal for detecting cybersickness through time domain feature extraction using naïve bayes. In *International Conference on Computer Engineering, Network and Intelligent Multimedia*, pp. 29–34, 2018. doi: 10.1109/CENIM.2018.8711320 2

[37] K. J. Mimnaugh, E. G. Center, M. Suomalainen, I. Becerra, E. Lozano, R. Murrieta-Cid, T. Ojala, S. M. LaValle, and K. D. Federmeier. Virtual Reality Sickness Reduces Attention During Immersive Experiences. *IEEE Transactions on Visualization and Computer Graphics*, 29(11):4394–4404, nov 2023. doi: 10.1109/TVCG.2023.3320222 1, 2, 3

[38] M. Mortaga, A. Brenner, and E. Kutafina. Towards interpretable machine learning in eeg analysis. *Studies in Health Technology and Informatics*, 283:32–38, Sept. 2021. doi: 10.3233/SHTI210538 3

[39] E. R. Muth. Motion and space sickness: Intestinal and

autonomic correlates. *Autonomic Neuroscience: Basic and Clinical*, 129(1–2):58–66, 2006. doi: 10.1016/j.autneu.2006.07.020 [2](#) [9](#)

[40] Y. Nam, Y. Kim, H. Kim, H. Ko, and K. Park. Automatic detection of nausea using bio-signals during immersing in a virtual reality environment. *International Conference of the IEEE Engineering in Medicine and Biology*, 2:2013–2015, 2001. IEEE Engineering in Medicine and Biology Society ; Conference date: 25-10-2001 Through 28-10-2001. [2](#)

[41] V. Napadow, J. D. Sheehan, J. Kim, L. T. Lacount, K. Park, T. J. Kapchuk, B. R. Rosen, and B. Kuo. The brain circuitry underlying the temporal evolution of nausea in humans. *Cerebral Cortex*, 23(4):806–813, 2013. doi: 10.1093/cercor/bhs073 [9](#)

[42] H. Oh and W. Son. Cybersickness and its severity arising from virtual reality content: A comprehensive study. *Sensors*, 22(4):1–26, 2022. doi: 10.3390/s22041314 [9](#)

[43] W. Y. Ong, C. S. Stohler, and D. R. Herr. Role of the prefrontal cortex in pain processing. *Molecular Neurobiology*, 56(2):1137–1166, 2019. doi: 10.1007/s12035-018-1130-9 [9](#)

[44] S. Palmisano, R. S. Allison, and J. Kim. Cybersickness in head-mounted displays is caused by differences in the user's virtual and physical head pose. *Frontiers in Virtual Reality*, 1:587698, Nov. 2020. doi: 10.3389/fvr.2020.587698 [2](#)

[45] A. Paszke, S. Gross, F. Massa, A. Lerer, J. Bradbury, G. Chanan, T. Killeen, Z. Lin, N. Gimelshein, L. Antiga, A. Desmaison, A. Kopf, E. Yang, Z. DeVito, M. Raison, A. Tejani, S. Chilamkurthy, B. Steiner, L. Fang, J. Bai, and S. Chintala. Pytorch: An imperative style, high-performance deep learning library, 2019. [4](#)

[46] F. Pedregosa, G. Varoquaux, A. Gramfort, V. Michel, B. Thirion, O. Grisel, M. Blondel, P. Prettenhofer, R. Weiss, V. Dubourg, J. Vanderplas, A. Passos, D. Cournapeau, M. Brucher, M. Perrot, and E. Duchesnay. Scikit-learn: Machine learning in Python. *Journal of Machine Learning Research*, 12:2825–2830, 2011. [4](#) [7](#)

[47] J. Polich. Updating p300: An integrative theory of p3a and p3b. *Clinical Neurophysiology*, 118(10):2128–2148, 2007. doi: 10.1016/j.clinph.2007.04.019 [1](#) [2](#) [3](#)

[48] F. H. Previc. Intravestibular balance and motion sickness. *Aerospace Medicine and Human Performance*, 89(2):130–140, 2018. doi: 10.3357/AMHP.4946.2018 [2](#)

[49] J. Reason and J. J. Brand. *Motion Sickness*. Academic Press, 1975. [2](#)

[50] J. T. Reason. Motion sickness adaptation: A neural mismatch model. *Journal of the Royal Society of Medicine*, 71(Nov):819–829, 1978. [2](#)

[51] G. E. Riccio and T. A. Stoffregen. An ecological theory of motion sickness and postural instability. *Ecological Psychology*, 3(3):195–240, 1991. doi: 10.1207/s15326969ecop0303_2 [2](#)

[52] O. Rosanne, D. Benesch, G. Kratzig, S. Paré, N. Bolt, and T. H. Falk. To pre-process or not to pre-process? on the role of eeg enhancement for cybersickness characterization and the importance of amplitude modulation features. *Frontiers in Virtual Reality*, 6(January):1–26, 2025. doi: 10.3389/fvr.2025.1468971 [2](#)

[53] P. J. Rousseeuw. Silhouettes: A graphical aid to the interpretation and validation of cluster analysis. *Journal of Computational and Applied Mathematics*, 20:53–65, 1987. doi: 10.1016/0377-0427(87)90125-7 [4](#)

[54] D. Saredakis, A. Szpak, B. Birckhead, H. A. Keage, A. Rizzo, and T. Loetscher. Factors associated with virtual reality sickness in head-mounted displays: A systematic review and meta-analysis. *Frontiers in Human Neuroscience*, 14(March), 2020. doi: 10.3389/fnhum.2020.00096 [2](#)

[55] R. Sclocco, J. Kim, R. G. Garcia, J. D. Sheehan, F. Beissner, A. M. Bianchi, S. Cerutti, B. Kuo, R. Barbieri, and V. Napadow. Brain circuitry supporting multi-organ autonomic outflow in response to nausea. *Cerebral Cortex*, 26(2):485–497, 2016. doi: 10.1093/cercor/bhu172 [9](#)

[56] D. A. Seminowicz and M. Moayedi. The dorsolateral prefrontal cortex in acute and chronic pain. *Journal of Pain*, 18(9):1027–1035, 2017. doi: 10.1016/j.jpain.2017.03.008 [9](#)

[57] D. Shimizu, K. Watanabe, and A. Dengel. Feature estimation of global language processing in eeg using attention maps. In *Proceedings of the Asian Conference on Computer Vision*, pp. 1706–1722, 2024. [3](#)

[58] Y. Song, Q. Zheng, B. Liu, and X. Gao. Eeg conformer: Convolutional transformer for eeg decoding and visualization. *IEEE Transactions on Neural Systems and Rehabilitation Engineering*, 31:710–719, 2023. doi: 10.1109/TNSRE.2022.3230250 [4](#) [5](#)

[59] K. Stanney, B. D. Lawson, B. Rokers, M. Dennison, C. Fidopiastis, T. Stoffregen, S. Weech, and J. M. Fulvio. Identifying causes of and solutions for cybersickness in immersive technology: Reformulation of a research and development agenda. *International Journal of Human-Computer Interaction*, 36(19):1783–1803, 2020. doi: 10.1080/10447318.2020.1828535 [2](#)

[60] M. Sundararajan, A. Taly, and Q. Yan. Axiomatic attribution for deep networks. In D. Precup and Y. W. Teh, eds., *International Conference on Machine Learning*, vol. 70 of *Proceedings of Machine Learning Research*, pp. 3319–3328. PMLR, 06–11 Aug 2017. [5](#)

[61] A. Szpak, S. C. Michalski, D. Saredakis, C. S. Chen, and T. Loetscher. Beyond feeling sick: The visual and cognitive aftereffects of virtual reality. *IEEE Access*, 7:130883–130892, 2019. doi: 10.1109/ACCESS.2019.2940073 [2](#)

[62] J. Teixeira, S. Miellet, and S. Palmisano. Unexpectedvection exacerbates cybersickness during hmd-based virtual reality. *Frontiers in Virtual Reality*, 3:1–14, Apr. 2022. doi: 10.3389/fvr.2022.860919 [2](#)

[63] J. Teixeira, S. Miellet, and S. Palmisano. Effects ofvection type and postural instability on cybersickness. *Virtual Reality*, 28(2):82, Mar. 2024. doi: 10.1007/s10055-024-00969-2 [2](#)

[64] N. Tian, P. Lopes, and R. Boulic. A review of cybersickness in head-mounted displays: Raising attention to individual susceptibility. *Virtual Reality*, 26(4):1409–1441, Dec. 2022. doi: 10.1007/s10055-022-00638-2 [2](#)

[65] L. van der Maaten and G. Hinton. Visualizing data using t-sne. *Journal of Machine Learning Research*, 9(86):2579–2605, 2008. [4](#)

[66] Y. Wei, Y. O. Okazaki, R. H. So, W. C. Chu, and K. Kitajo. Motion sickness-susceptible participants exposed to coherent rotating dot patterns show excessive n2 amplitudes and impaired theta-band phase synchronization. *NeuroImage*, 202(July):116028, 2019. doi: 10.1016/j.neuroimage.2019.116028 [2](#)

[67] G. F. Woodman. A brief introduction to the use of event-related potentials in studies of perception and attention. *Attention, Perception & Psychophysics*, 72(8):2031–2046, 2010. doi: 10.3758/APP.72.8.2031 [2](#)

[68] J. Wu, Q. Zhou, J. Li, X. Kong, and Y. Xiao. Inhibition-related n2 and p3: Indicators of visually induced motion sickness (vims). *International Journal of Industrial Ergonomics*, 78(June):102981, 2020. doi: 10.1016/j.ergon.2020.102981 [2](#)

[69] L. Xuhong, Y. Grandvalet, and F. Davoine. Explicit inductive bias for transfer learning with convolutional networks. In *International conference on machine learning*, pp. 2825–2834. PMLR, 2018. [6](#)

[70] Y. Yan, H. Zhou, L. Huang, X. Cheng, and S. Kuang. A novel two-stage refine filtering method for eeg-based motor imagery classification. *Frontiers in neuroscience*, 15:657540, 2021. [3](#)

[71] A. H. X. Yang, N. Kasabov, and Y. O. Cakmak. Machine learning methods for the study of cybersickness: a systematic review. *Brain Informatics*, 9(1), 2022. doi: 10.1186/s40708-022-00172-6 [2](#) [3](#)

[72] A. H. X. Yang, N. K. Kasabov, and Y. O. Cakmak. Prediction and detection of virtual reality induced cybersickness: a spiking neural network approach using spatiotemporal eeg brain data and heart rate variability. *Brain Informatics*, 10(1), 2023. doi: 10.1186/s40708-023-00192-w [9](#)

[73] R. Yang and E. Modesitt. Vit2eeg: leveraging hybrid pretrained vision transformers for eeg data. *arXiv preprint arXiv:2308.00454*, 2023. [5](#)

[74] C. Yildirim. A review of deep learning approaches to eeg-based classification of cybersickness in virtual reality. *IEEE International Conference on Artificial Intelligence and Virtual Reality, AIVR 2020*, p. 351–357, 2020. doi: 10.1109/AIVR50618.2020.00072 [2](#)

[75] Y.-H. Yu, P.-C. Lai, L.-W. Ko, C.-H. Chuang, B.-C. Kuo, and C.-T. Lin. An eeg-based classification system of passenger's motion sickness level by using feature extraction/selection technologies. In *International Joint Conference on Neural Networks*, pp. 1–6, 2010. doi: 10.1109/IJCNN.2010.5596739 [2](#)

[76] J. Zhou, Y. Wang, X. Luo, P. B. Fitzgerald, R. F. Cash, B. M. Fitzgibbon, and X. Che. Revisiting the effects of rtms over the dorsolateral prefrontal cortex on pain: An updated systematic review and meta-analysis. *Brain Stimulation*, 17(4):928–937, 2024. doi: 10.1016/j.brs.2024.07.011 [9](#)

SUPPLEMENTAL MATERIAL

7.1 Additional plots

We include additional integrated gradient plots from different random seed experiment trials in Figs. 8 and 9. The plots for the trial with channel order re-arranged is in Fig. 7. LLPf remains the electrode channel with highest attribution across the models for classifying sickness.

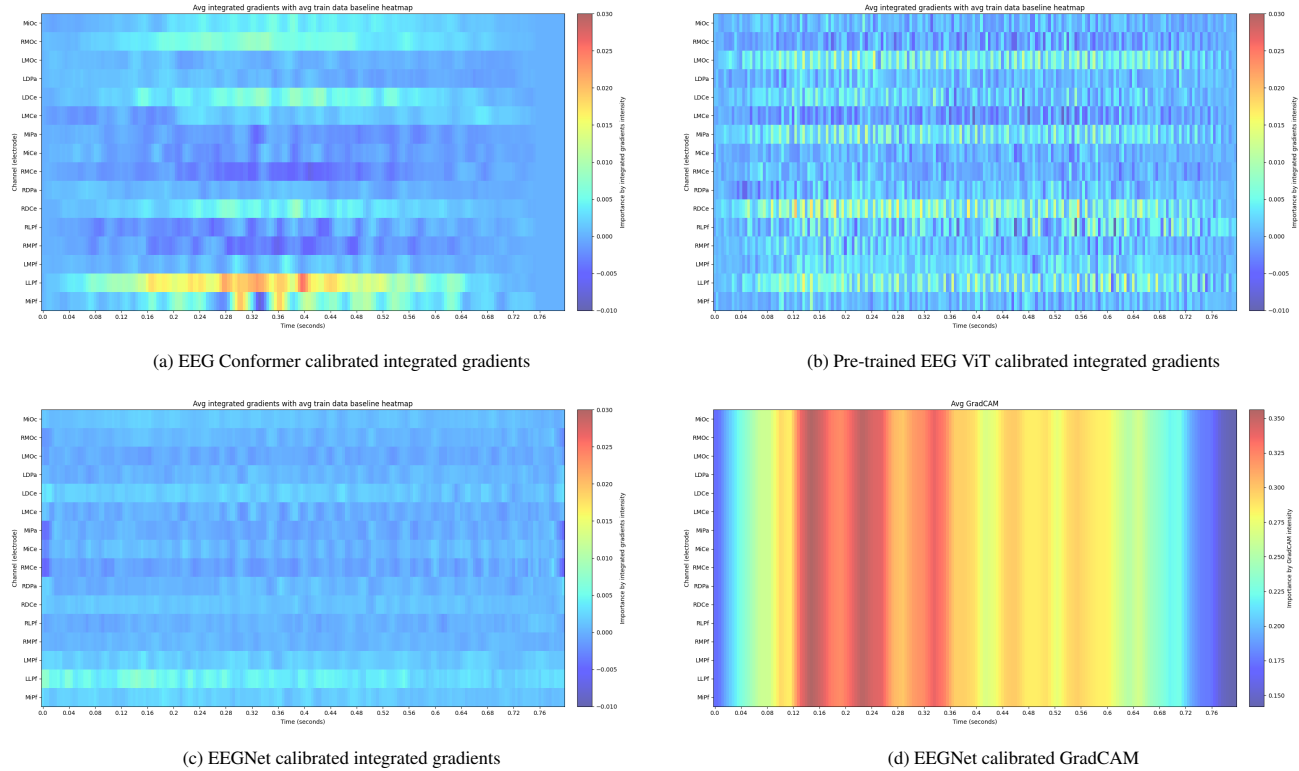


Figure 7: Integrated gradients for calibrated models averaged over sick data from balanced accuracy $> 75\%$ subjects and GradCAM for EEGNet trained with different channel order.

7.2 Using different SSQ symptom as label

To verify our method works for other kinds of patterns, “Difficulty focusing,” a different SSQ symptom, was used to create binary classification labels in Fig. 10. The top attribution channels are RDCe and MiPf this time, highlighting different electrodes are useful for detecting “Difficulty focusing”.

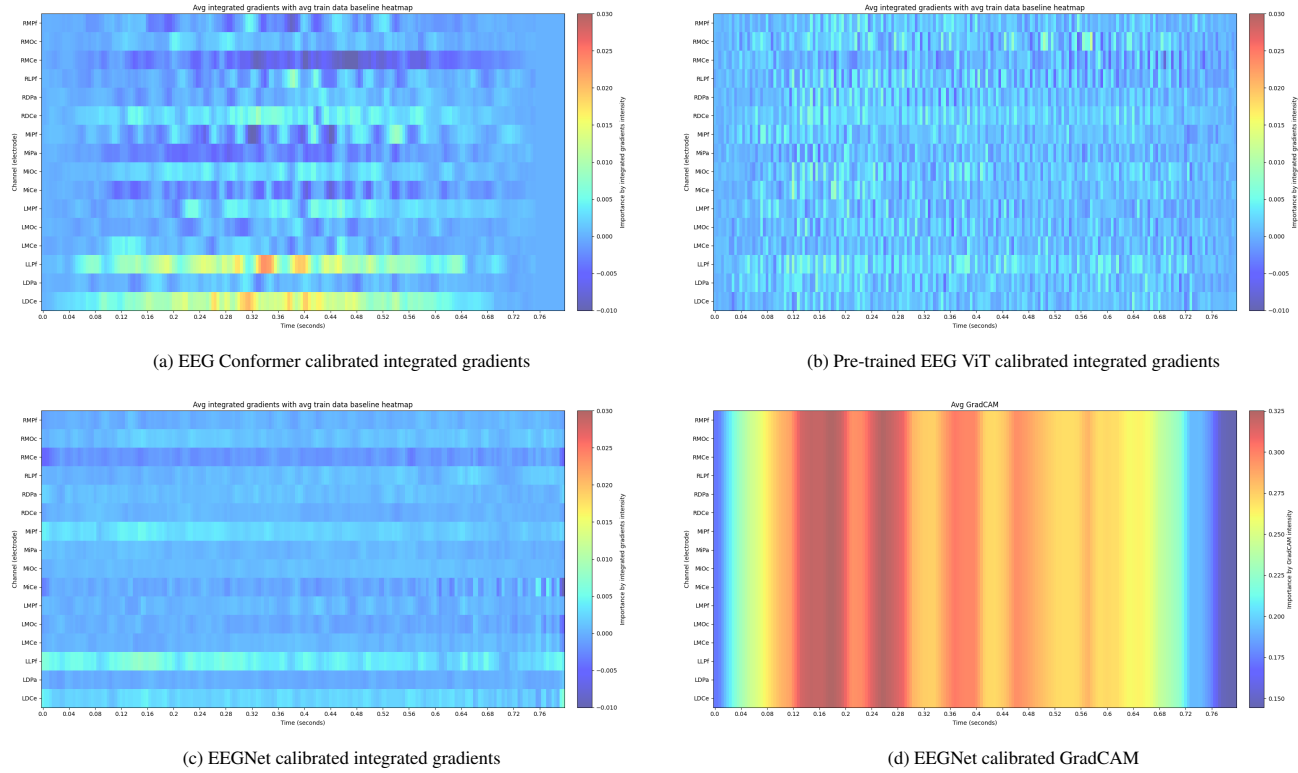


Figure 8: Integrated gradients for calibrated models averaged over sick data from balanced accuracy $> 75\%$ subjects and GradCAM for EEGNet with random seed 3.

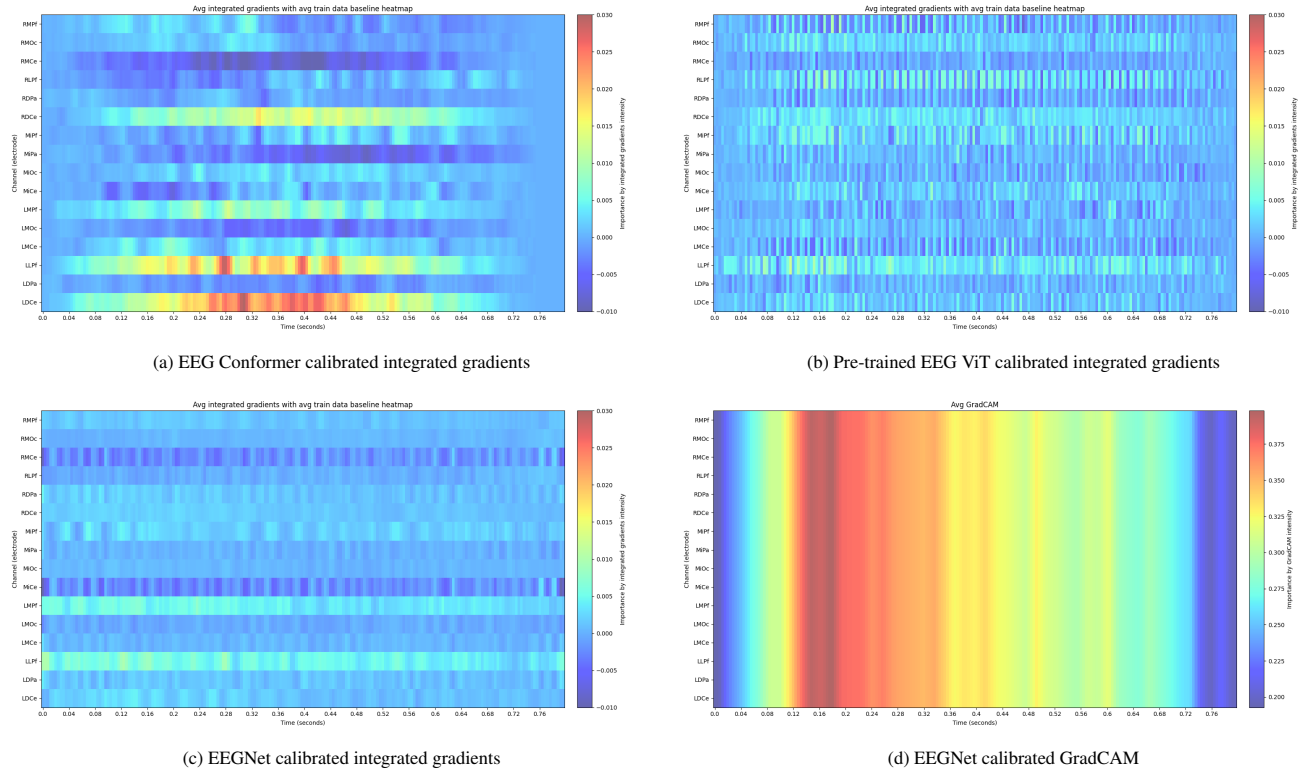


Figure 9: Integrated gradients for calibrated models averaged over sick data from balanced accuracy $> 75\%$ subjects and GradCAM for EEGNet with random seed 2.

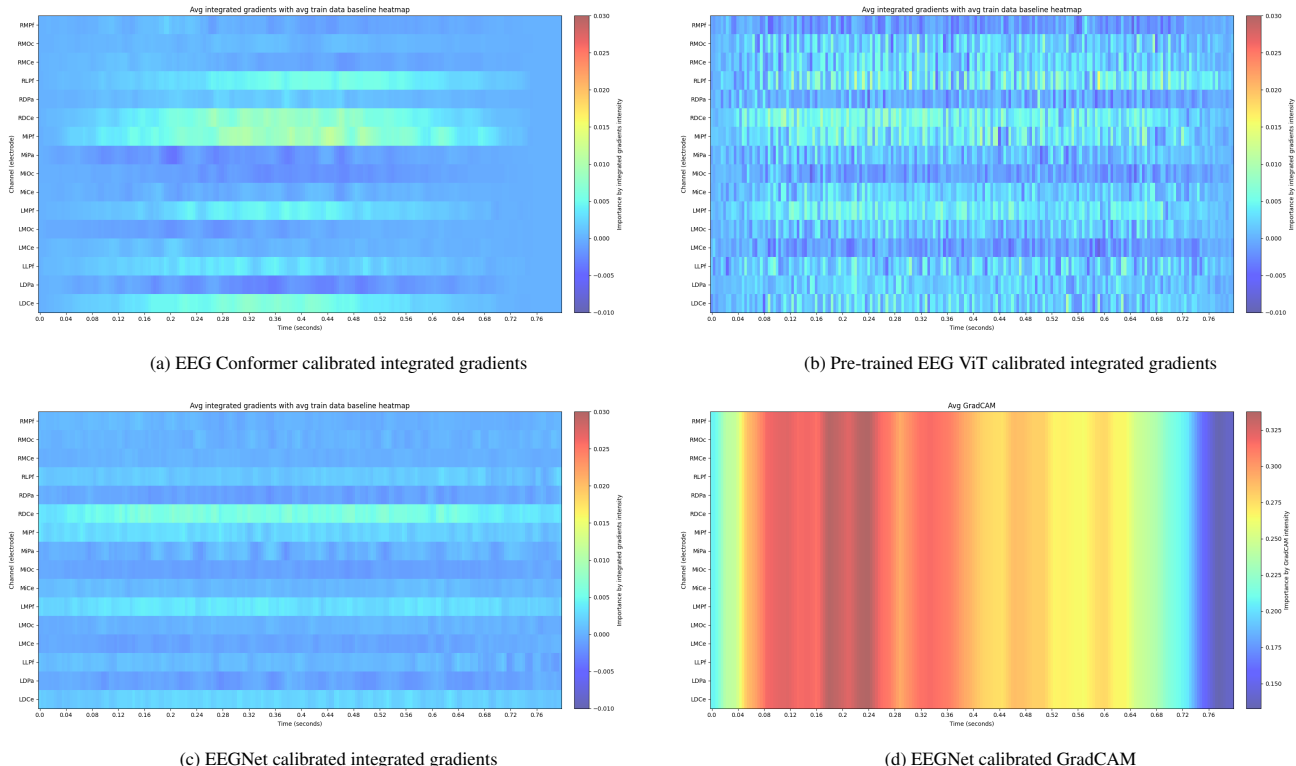


Figure 10: Integrated gradients for calibrated models averaged over sick data from balanced accuracy $> 75\%$ subjects and GradCAM for EEGNet for “Difficulty focusing” labels.